Three-dimensional ellipsoidal discrete element modeling of granular materials and its coupling with finite element facets

Beichuan Yan, Richard A. Regueiro and Stein Sture

*Department of Civil, Environmental and Architectural Engineering,
University of Colorado at Boulder, Boulder, Colorado, USA*

Abstract

Purpose – The purpose of this paper is to develop a discrete element (DE) and multiscale modeling methodology to represent granular media at their particle scale as they interface solid deformable bodies, such as soil-tool, tire, penetrometer, pile, etc., interfaces.

Design/methodology/approach – A three-dimensional ellipsoidal discrete element method (DEM) is developed to more physically represent particle shape in granular media while retaining the efficiency of smooth contact interface conditions for computation. DE coupling to finite element (FE) facets is presented to demonstrate initially the development of overlapping bridging scale methods for concurrent multiscale modeling of granular media.

Findings – A closed-form solution of ellipsoidal particle contact resolution and stiffness is presented and demonstrated for two particle, and many particle contact simulations, during gravity deposition, and quasi-static oedometer, triaxial compression, and pile penetration. The DE-FE facet coupling demonstrates the potential to alleviate artificial boundary effects in the shear deformation region between DEM granular media and deformable solid bodies.

Research limitations/implications – The research is being extended to couple more robustly the ellipsoidal DEM code and a higher order continuum FE code via overlapping bridging scale methods, in order to remove dependence of penetration/shear resistance on the boundary placement for DE simulation.

Practical implications – When concurrent multiscale computational modeling of interface conditions between deformable solid bodies and granular materials reaches maturity, modelers will be able to simulate the mechanical behavior accounting for physical particle sizes and flow in the interface region, and thus design their tool, tire, penetrometer, or pile accordingly.

Originality/value – A closed-form solution for ellipsoidal particle contact is demonstrated in this paper, and the ability to couple DE to FE facets.

Keywords Mechanical behavior of materials, Modeling, Finite element analysis

Paper type Research paper

1. Introduction

The discrete element method (DEM) has been used to investigate the mechanical behavior of assemblies of granular materials since the introduction of the method (Cundall and Strack, 1979). Research results have demonstrated that the method can simulate certain aspects of granular material response, such as strength, stiffness, dilatancy, influence of intermediate principal stress and localized deformation, even under conditions like low effective stress state in the Space Shuttle (Zhang, 1996, Gong, 2001). The DEM has also been found to be an extremely valuable tool to obtain the

micromechanical details, such as fabric and structure, of granular materials (Rothenburg and Bathurst, 1992; Ng, 1993, 1994, 1999; Ng and Fang, 1995). In addition to the research into micromechanics of granular materials, many other practical applications using DEM were presented in an international conference on DEMs (Cook and Jensen, 2002). These include the formation of muck piles resulting from rock blasting in mining, problems of particle-fluid systems such as liquefaction analysis and wet granular flow, amongst others.

A disadvantage of the DEM is that it can lead to computational times and memory demands beyond the capacity of many modern computers (even massively parallel systems). This is a result of solving contact detection algorithms for many particles (especially in three dimensions), and also the small time step required to maintain stability for the traditional explicit central time difference scheme used to integrate the balance of linear and angular momemtum equations for all particles. For example, in a $1 \, \text{cm}^3$ fine-grained soil volume (particle size range 1-100 mm) there could be approximately 5×10^{12} particles, which is beyond the capacity of most modern computers.

Part of the reason for not being able to model the flow and deformation of granular materials in a physically based manner within one computational framework is that the length scale of the application is usually much larger than the length scale of the particles composing the granular material, e.g. 100 mm diameter quartz particles of a sand sheared by a 10 cm diameter steel pile penetrating 1 m deep in the ground, which is four orders of magnitude difference in scale (requiring around 10^{10} particles to simulate). As a result, it is not feasible to simulate computationally the heterogeneous, localized deformation, flow response in the engineering application of interest involving granular materials using a pure particle-based materials modeling approach.

Granular materials may transition in an instant from deforming like a solid to flowing like a fluid and vice versa. Examples of such physical transition are the flow of quartz grains at the tip of a driven steel pile, and the flow of agricultural grains from the bulk top region through the bottom chute in a silo, for instance. These examples each involve material regions where relative neighbor particle motion is "large" (flowing like a fluid) and regions where relative neighbor particle motion is "small" (deforming like a solid). This is particularly true for applications involving granular material compression and shear by a deformable solid body, such as tire/track, tool, cone penetrometer, or pile interfacing granular material like sand.

For certain applications, to achieve computational efficiency while maintaining high material model resolution in spatial domains of interest, coupling discrete element (DE) and finite element (FE) methods is one approach. This combination of FEs with DE is especially effective for problems where standard continuum FE are only adequate to model part of the analysis domain, whereas DE is more accurate to treat other areas. Examples of such problems can be found in the interaction of solids and structures with granular media, such as the pile driving process mentioned above. Treatment of overlap between DE and the boundary of a continuum subdomain discretized with FE involves properly transferring force, moment and energy between the two different domains.

A few approaches have coupled DE and FE for modeling deformation and flow of dense dry granular materials accounting for the physical particle size, i.e. truly micromechanically coupled models (Negi *et al.*, 1999; Han *et al.*, 2000; Kremmer and Favier, 2001; Komodromos and Williams, 2002, 2004; Nakashima and Oida, 2004; Onate and Rojek, 2004; Cheng *et al.*, 2005). These methods approach the coupling issue,

however, as a contact/interface problem between two materials (discrete particles for granular material and FE facets for deformable solid) and not coupling different numerical model representations of the same material (i.e. a granular material), which an approach coupling particle and continuum representations of the same material should do. The interface/contact problem addressed by these authors is still relevant at the interface between particles and a deformable solid, but we focus on the problem of resolving the granular material behavior using DE in the interface region, transitioning to continuum FE spatially further from the interface to achieve computational efficiency while properly representing boundary conditions (BCs) on the DE domain.

Multiscale approaches have gained attention in materials science in recent years, especially in the research on nanoscale mechanics and materials. For lattice-structured materials, it attempts to overcome the difficulties that arise from high demand on computational resources and seeks to limit molecular dynamics (MD) in localized regions where atomic-scale dynamics are important while allowing continuum simulations everywhere else (Liu *et al.*, 2006). Similar situations occur in the research of granular material problems aforementioned.

The goal of this study can be divided into two parts. First, a three-dimensional (3D) DE code is developed with the capacity to operate ellipsoidal particles with translational and rotational degrees of freedom and to handle rigid BCs. Fundamental mechanical behavior of particle contact in normal and tangential directions is investigated. Numerical tests with up to several thousand particles, including isotropic, oedometer (uniaxial strain) and triaxial compression, are performed to study macroscopically mechanical behavior of granular material. In this research, a generic ellipsoidal particle representation and contact resolution alogrithm are presented and implemented, which follows the approximation of an axis-symmetric ellipsoidal shape (Wang *et al.*, 1999; Ng and Fang, 1995; Hopkins, 2002; Kuhn, 2003; Ng, 2004; Hopkins, 2004; Johnson *et al.*, 2004) At the contact between two particles, Hertz's nonlinear elastic model is employed for the normal behavior and Mindlin's history-dependent stick/slip model combined with Coulomb's friction model is employed for the tangential behavior.

Second, a coupled multiscale modeling approach for granular materials is proposed and implemented, numerical examples of pile penetration with artificial BC and coupled FE facets are compared to verify the method.

An outline of the remainder of the paper is as follows: section 2 describes the ellipsoidal DEM; section 3 presents DEM examples; section 4 describes a DE-FE facet coupling method; section 5 presents DE-FE coupling simulations; and section 6 conclusions.

2. Ellipsoidal discrete element model
2.1 Governing equations, integration scheme and contact interface
The translational and rotational motion of ellipsoidal particles in 3D space is described by means of standard rigid body dynamics, namely, equations of balance of linear and angular momentum. For the ith particle we have

$$m_i \ddot{\boldsymbol{u}}_i = \boldsymbol{F}_i \tag{1}$$

$$I_i \ddot{\boldsymbol{\theta}}_i = \boldsymbol{M}_i \tag{2}$$

where $\boldsymbol{u}$ is the particle centroid displacement in an inertial coordinate frame, which we define as global coordinate system – (GCS); $\boldsymbol{\theta}$, the spatial orientation vector of the

particle; m, the particle mass; I, the moment of inertia; F, the resultant force; and M, the resultant moment about the principal axes of inertial frame. Equation (2) holds in GCS, but it is much more convenient to use it in a co-rotational local coordinate system (LCS) embedded at each particle in that tensor of inertia is constant in LCS. It is desirable to evaluate each variable of Equation (2) in LCS consistently and convert them into GCS in calculating rotations in GCS.

A particle in a granular assembly is subjected to contact forces, external forces such as gravity and boundary forces, and damping forces. For the ith particle the equation of motion can be expressed including viscous damping as:

$$M_i a_i + C_i v_i + P_i = F_i \tag{3}$$

where M_i and C_i are the generalized mass and viscous damping matrices, respectively, as:

$$M_i = \begin{bmatrix} m_i & 0 & 0 & 0 & 0 & 0 \\ 0 & m_i & 0 & 0 & 0 & 0 \\ 0 & 0 & m_i & 0 & 0 & 0 \\ 0 & 0 & 0 & I_i & 0 & 0 \\ 0 & 0 & 0 & 0 & I_i & 0 \\ 0 & 0 & 0 & 0 & 0 & I_i \end{bmatrix} \tag{4}$$

$$C_i = \alpha_1 M_i \tag{5}$$

where α_1 is the coefficient of mass proportional damping. a_i and v_i are generalized acceleration and velocity vectors, respectively, as:

$$v_i^T = \left[v_{x(i)}, v_{y(i)}, v_{z(i)}, \omega_{x(i)}, \omega_{y(i)}, \omega_{z(i)} \right]$$
$$a_i^T = \left[\dot{v}_{x(i)}, \dot{v}_{y(i)}, \dot{v}_{z(i)}, \dot{\omega}_{x(i)}, \dot{\omega}_{y(i)}, \dot{\omega}_{z(i)}) \right] \tag{6}$$

where ω is the angular velocity. P_i are the generalized contact loads, including force vectors and moment vectors, F_i the generalized external loads and $C_i v_i$ the mass proportional (background) damping forces. The generalized contact loads vector is written as:

$$P_i^T = \left[\sum_{j=1}^{n_c} F_x^{j,i}, \sum_{j=1}^{n_c} F_y^{j,i}, \sum_{j=1}^{n_c} F_z^{j,i}, \sum_{j=1}^{n_c} M_x^{j,i}, \sum_{j=1}^{n_c} M_y^{j,i}, \sum_{j=1}^{n_c} M_z^{j,i} \right] \tag{7}$$

where $F_x^{j,i}$, $F_y^{j,i}$ and $F_z^{j,i}$ are the scalar components of the contact forces exerted on the ith particle by the jth particle, and $M_x^{j,i}$, $M_y^{j,i}$ and $M_z^{j,i}$ are, similarly, the scalar components of contact moments. n_c denotes the number of contacts for the ith particle.

Equation of motion (3) is integrated in time using the central difference method due to its simplicity (no need for iteration and consistent tangent) and second-order accuracy. Assuming mass proportional damping of the form $C = \alpha_1 M$, with proportionality parameter α_1, the following midstep velocity update is obtained as:

$$v_{n+1/2} = \frac{1 - \alpha_1 \Delta t/2}{1 + \alpha_1 \Delta t/2} v_{n-1/2} + \frac{1}{1 + \alpha_1 \Delta t/2} \Delta t M^{-1}[F_n - P_n] \qquad (8)$$

where n denotes the nth time, and Δt is the time step. Equation (8) can be evaluated at any time n to obtain the midstep velocity $v_{n+1/2}$, and then the displacement.

The theoretical critical time step obtained from linear stability analysis can be used to estimate the time step as:

$$\Delta t < 2/\omega_{\max} = 2\sqrt{\frac{m}{k}} \qquad (9)$$

where m/k is a minimum, resulting from the combination of smallest particle mass and largest interparticle stiffness at contact. It is noted from Equation (29) that this interparticle stiffness is a variable depending on particle overlap magnitude. Actual time step could be a fraction of this number, for example, 1-10 percent adopted for dynamic simulations in this paper.

When the method is used to solve static or quasi-static problems, a dynamic relaxation (DR) procedure (Key, Stone, and Krieg, 1980; Underwood, 1983) is performed to achieve convergence to the static solution. DR is often used in explicit codes to obtain static or quasi-static solutions. The basic idea is to apply the load very slowly and solve the dynamic system equations with enough damping so that oscillations are minimized. In DR, only P and F must represent the physics, while C and M are fictitious values such that the static solution is obtained in a minimum number of steps. DR is applicable, in general, for quasi-static loading of dense granular materials, in which inertial particle forces and moments are negligible.

The mass proportional viscous damping $C = \alpha_1 M$ can be referred to background damping, which is sometimes necessary to apply to non-contacting particles to dissipate their energy during DR. Aside from the background damping, interparticle contact damping is essential to model the mechanical interaction between particles. This is especially true for dynamic problems where interparticle collisions dominate the kinetic energy dissipation. For physical dynamic problems, we apply only interparticle normal contact damping and tangential friction without involving any background damping. The contact interface is illustrated in Figure 1, characterized by
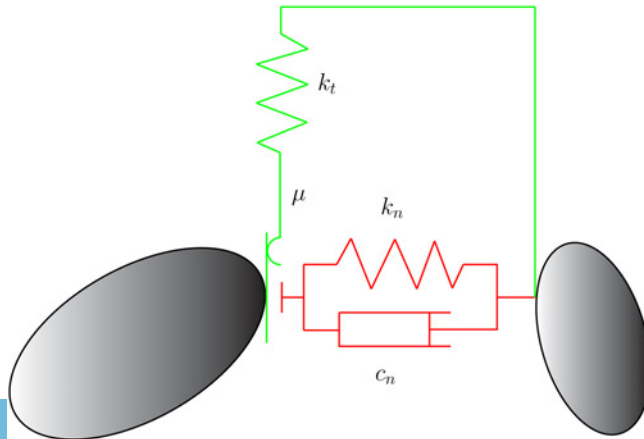

Figure 1.
Model of contact interface

the normal and tangential stiffness k_n and k_t, respectively, friction coefficient μ, and the normal contact damping coefficient c_r.

The normal contact damping force between particles is assumed to be of viscous type and given by:

$$\boldsymbol{F}_d = c_r \boldsymbol{v}_r \tag{10}$$

where $\boldsymbol{v}_r$ is the normal relative velocity vector of the centers of the two particles in contact, defined by:

$$\boldsymbol{v}_r = (\dot{\boldsymbol{u}}_2 - \dot{\boldsymbol{u}}_1) \cdot \boldsymbol{n} \tag{11}$$

where $\boldsymbol{n}$ is the contact normal.

The normal damping coefficient c_r (Onate and Rojek, 2004) can be taken as a fraction of the critical damping C_{cr} for the system of two rigid bodies with masses m_1 and m_2, connected with a spring of stiffness k_n (Taylor and Preece, 1992):

$$C_{cr} = 2\sqrt{\frac{m_1 m_2 k_n}{m_1 + m_2}} \tag{12}$$

$$c_r = \xi C_{cr} \tag{13}$$

where ξ is called damping ratio, which is usually 1-5 percent. In the tangential direction of contact between particles, friction will dissipate energy.

In the tangential direction of the contact between particles, friction plays the role to dissipate energy. Usually, it is necessary to apply damping for the case of static friction and the tangential critical damping can be similarly given by:

$$C_{cr} = 2\sqrt{\frac{m_1 m_2 k_t}{m_1 + m_2}} \tag{14}$$

2.2 Contact geometry of ellipsoids
Ellipsoidal particles are chosen as the particle shapes in the 3D DE computation. First, they can represent a wide range of 3D objects: spherical, bulky, platy or even needlelike, as shown in Figure 2. Second, their contact geometries can be obtained mathematically using closed-form equations. Third, the most important, for granular materials with non-spherical interlocking grains (e.g. not spherical glass beads), non-physical particle rotations can be avoided that lead to low shear resistance (Wang *et al.*, 1999). Some researchers have added a rolling friction factor (Vu-Quoc *et al.*, 2004) to alleviate this non-physical low shear resistance representation when using spherical particles. We choose to use a more physically-representative particle shape: an ellipsoidal particle.

To calculate the contact properties between two generic ellipsoids, Lin and Ng proposed two different contact resolution algorithms (Lin and Ng, 1995). One is based on a geometric potential concept resulting in a 6th order polynomial equation and the other on a common normal concept resulting in a set of six equations. By comparison with analytical results on two spheres, they concluded that the geometric potential algorithm has a better accuracy and efficiency than the common normal one although
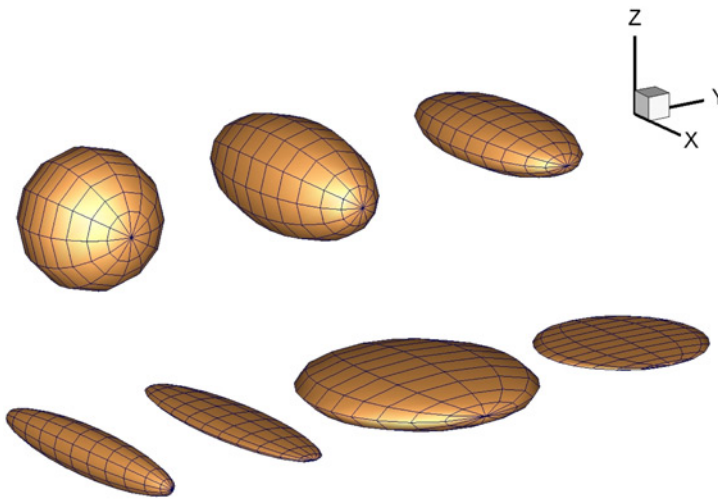
Notes: Particle surfaces are analytically smooth and the apparent tessellation is a
product of the visualization software

Figure 2.
Various shaped ellipsoids

it does not guarantee that the surface normals at the two contact points on each
ellipsoid are parallel to each other. This paper follows the algorithm based on
geometric potential.

An ellipsoid in 3D space is determined by the following parameters: position of the
center (x_0, y_0, z_0), length of three axes (a, b, c) and orientation of the three axes, which is
expressed as three vectors of direction cosine $(l1, m1, n1)$, $(l2, m2, n2)$, $(l3, m3, n3)$.
Among the last nine parameters only three of them are independent.

In general, the algebraic expression for the surface of an ellipsoidal particle in 3D
Cartesian coordinate space is shown as follows:

$$f_i = a_1^i x^2 + a_2^i y^2 + a_3^i z^2 + a_4^i xy + a_5^i yz + a_6^i zx + a_7^i x + a_8^i y + a_9^i z + a_{10}^i = 0, i = 1, 2 \tag{15}$$

where i is the particle index of one of two particles in a contact pair, and a_1 to a_{10} are the
ten coefficients describing a particle surface.

Figure 3 illustrates contact between two ellipsoids. Point P1 is a point on the surface
of particle 1 and it has the deepest penetration into particle 2, and point P2 is a point on
the surface of particle 2 and has the deepest penetration into particle 1. The penetration
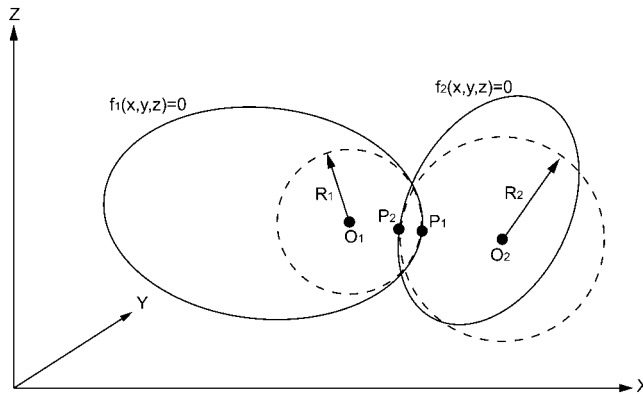between two particles is defined as the length of line segment between points P1 and P2.

To acquire the coordinates of point P1, the following extreme value problem is
introduced to seek f_2's minimum with a constraint condition $f_1 = 0$:

$$L(x, y, z, \lambda) \equiv f_2(x, y, z) + \lambda f_1(x, y, z) \tag{16}$$

where f_1 and f_2 are functions of the surfaces corresponding to Equation (15), and λ is
the Lagrange multiplier (Sokolnikoff, 1939).

To solve the extreme value problem, the vanishing of the total differential is the
necessary condition:

$$\frac{\partial L(x,y,z,\lambda)}{\partial x} = 0, \quad \frac{\partial L(x,y,z,\lambda)}{\partial y} = 0$$
$$\frac{\partial L(x,y,z,\lambda)}{\partial z} = 0, \quad \frac{\partial L(x,y,z,\lambda)}{\partial \lambda} = 0 \tag{17}$$

These PDE's lead to a sixth order polynomial equation of λ (Gong, 2001). When λ is determined, the spatial coordinate of point P1 can be acquired. A similar procedure can be used to obtain point P2.

As there is no analytical root-finding solution for a sixth order polynomial, a robust and precise numerical procedure must be selected. According to Numerical Recipes (Press, 2007), several polynomial root-finding algorithms are available, such as Muller's method, Laguerre's method and eigenvalue method. The basic idea of eigenvalue method is that the eigenvalues of a matrix A are the roots of the "characteristic polynomial" $P(x) = det[A - xI]$ such that some efficient eigenvalue methods can be utilized to find the roots of arbitrary polynomials. The eigenvalue method is selected in this research and is proved to be quite robust in detecting contact between any two ellipsoidal surfaces.

For ease of numerical implementation, we assume the contact area is circular, which is reasonable for stiff particles. The contact geometry between two ellipsoids can be approximated by assuming two osculating spheres passing through the contact point on each ellipsoid surface, which is shown in Figure 3.

An ellipsoidal surface from Equation (15) can be regarded as a generic space surface:

$$z = f(x,y) \tag{18}$$

The following variables are introduced:

$$r = \frac{\partial^2 z}{\partial x^2}, \quad s = \frac{\partial^2 z}{\partial x \partial y}, \quad t = \frac{\partial^2 z}{\partial y^2}, \quad p = \frac{\partial z}{\partial x}, \quad q = \frac{\partial z}{\partial y}, \quad h = \sqrt{1 + p^2 + q^2} \tag{19}$$

such that the second fundamental coefficients are expressed:

$$L = \frac{r}{h}, \quad M = \frac{s}{h}, \quad N = \frac{t}{h} \tag{20}$$

There are directions at a surface point P along which the normal curvature at P has maximum or minimum values, namely, principal directions at P. The principal curvatures at P are the normal curvatures at P along the principal directions. The principal curvature radii are given by the roots of a quadratic equation (Lipschutz, 1969; Somasundaram, 2004):

$$(rt - s^2)R^2 + h[2pqs - (1 + p^2)t - (1 + q^2)r]R + h^4 = 0 \tag{21}$$

where the two roots are denoted by R_1 and R_2. The mean curvature radius of the osculating sphere is given by (Lipschutz, 1969):

$$R = \frac{2R_1 R_2}{R_1 + R_2} \tag{22}$$

2.3 Constitutive contact relationships
Particle contacts are assumed to be elastic and frictional such that elastic contact theory can be utilized. The Hertz-Mindlin model (Hertz, 1882; Mindlin, 1949) is a widely used particle contact constitutive model in DE models, and includes nonlinear elasticity and slip. Sometimes a simple Coulomb friction model can be employed to evaluate tangential stick-slip conditions.

Hertz (1882) assumed the following conditions:

(1) Contact shape can be represented by a quadratic surface.

(2) Solution for a semi-infinite elastic half space with a point force BC is applicable at contact.

(3) The two particle surfaces are perfectly smooth.

Under these conditions the distribution of contact pressure for two spheres is:

$$p(r) = \frac{3P}{2\pi a^2} \sqrt{1 - \left(\frac{r}{a}\right)^2} \tag{23}$$

where P is the normal force, a is the radius of contact area, and r is the contact surface coordinate. Figure 4(a) illustrates the contact model between two spheres, such that:

$$a = \left(\frac{3PR_0}{4E_0}\right)^{1/3} = (\rho R_0)^{1/2} \tag{24}$$

$$\frac{1}{R_0} = \frac{1}{R_1} + \frac{1}{R_2} \tag{25}$$

$$\frac{1}{E_0} = \frac{1 - \nu_1^2}{E_1} + \frac{1 - \nu_2^2}{E_2} \tag{26}$$

where R_1 and R_2 are the radii of the two spheres, E_1, E_2, ν_1, ν_2 are Young's modulus and Poisson's ratio, respectively. The relationship between normal load P and normal
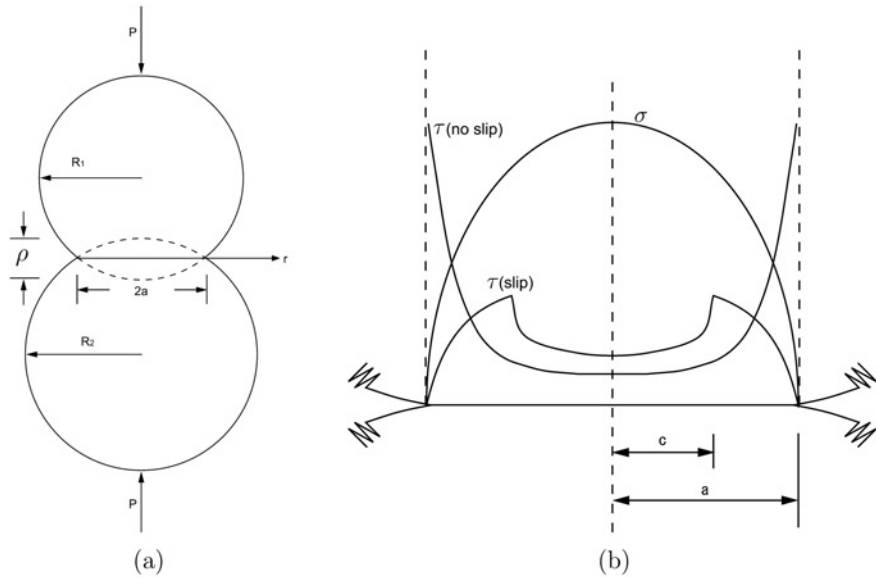
Figure 4.
Hertz-Mindlin contact
model

Notes: (a) Hertz model and (b) Mindlin model

displacement ρ is:

$$\rho = R_0^{-1/3} \left(\frac{3P}{4E_0} \right)^{2/3} \tag{27}$$

$$P = \frac{4}{3} E_0 R_0^{1/2} \rho^{3/2} \tag{28}$$

and the normal stiffness k_n is

$$k_n = \frac{dP}{d\rho} = (6PR_0 E_0^2)^{1/3} \tag{29}$$

History dependence of tangential displacement on normal and tangential loads was studied by Mindlin and Deresiewicz for various cases (Mindlin, 1949; Mindlin *et al.*, 1952; Mindlin and Deresiewicz, 1953) and they drew the conclusion that "Not only do the changes in stresses and displacements depend upon the initial state of loading, but also upon the entire past history of loading and the instantaneous relative rates of change of the normal and tangential forces". Ten different cases with complicated conditions and expressions for the tangential stiffness were presented (Mindlin and Deresiewicz, 1953). However, we only implement three of them where the normal force is held constant because it is difficult to keep track of every history state in order to distinguish all the ten cases when the DEM performs calculation of hundreds of thousands of steps.

(1) *No slip.* If there is no slip on the contact surface, the relative tangential displacement is proportional to the applied tangential force:

$$\delta = \frac{2 - \nu}{4Ga} T \qquad (30)$$

where T is the tangential force, and G is the shear modulus.

(2) *Partial slip.* In order to avoid a singularity in traction (which would be unphysical), slip is allowed at non-zero tangential force. Slip progresses radially inward from the edge of the contact area, producing a slip-stick region as shown in Figure 4(b).

The radius of the stick portion is:

$$c = a \left(1 - \frac{T}{\mu P} \right)^{1/3} \qquad (31)$$

where μ is the intersphere constant coefficient of static friction.

The relationship between the relative tangential displacement δ and tangential force T is:

$$\delta = \frac{3(2 - \nu)\mu P}{8Ga} \left[1 - \left(1 - \frac{T}{\mu P} \right)^{2/3} \right] \qquad (32)$$

$$T = \mu P \left\{ 1 - \left[1 - \frac{8Ga\delta}{3(2 - \nu)\mu P} \right]^{3/2} \right\} \qquad (33)$$

The tangential stiffness of the contact is:

$$k_t = \frac{dT}{d\delta} = \frac{4Ga}{2 - \nu} \left[1 - \frac{8Ga\delta}{3(2 - \nu)\mu P} \right]^{1/2} \qquad (34)$$

(3) *Decreasing tangential force.* When tangential force decreases from a peak value $T_s (0 < T_s < \mu P)$, the tangential stiffness of the contact is different from that in the case of an increasing tangential force (i.e. different loading and unloading response). In this case:

$$\delta = \frac{3(2 - \nu)\mu P}{8Ga} \left[2 \left(1 - \frac{T_s - T}{2\mu P} \right)^{2/3} - \left(1 - \frac{T_s}{\mu P} \right)^{2/3} - 1 \right] \qquad (35)$$

$$T = T_s - 2\mu P \left\{ 1 - \frac{\sqrt{2}}{4} \left[1 + \left(1 - \frac{T_s}{\mu P} \right)^{2/3} + \frac{8Ga\delta}{3(2 - \nu)\mu P} \right]^{3/2} \right\} \qquad (36)$$

and the tangential stiffness of the contact is:

$$k_t = \frac{dT}{d\delta} = \frac{2\sqrt{2}Ga}{2 - \nu} \left[1 + \left(1 - \frac{T_s}{\mu P} \right)^{2/3} + \frac{8Ga\delta}{3(2 - \nu)\mu P} \right]^{1/2} \qquad (37)$$

2.4 General features of ELLIP3D

ELLIP3D is a 3D DEM simulation code written in C++ with object-oriented design. It calculates particle motions in terms of translational and rotational degrees of freedom based on the second law of Newton, described in Equations (1) and (2). Particle rotations are calulated in LCS and converted into GCS. Particle contact resolution algorithm is based on the geometric potential concept, and an eigenvalue method is used to seek roots for the resulting sixth order polynomial. In determining the principal curvature radii at an ellipsoidal surface point through Equation (21), singularity along ellipsoid equators is carefully avoided by coordinate switching. Both dynamic and quasi-static simulations are performed, and the code is proved to be robust. The average number of contact resolution calculations per second is approximately 10^4/sec on a single AMD 3.2 GHz CPU.

3. Discrete element method simulation examples

This section demonstrates numerical DEM examples to verify the ellipsoidal contact detection algorithm, interparticle constitutive behavior, and quasi-static and dynamic simulation capabilities. The parameters for the particles are for typical quartz sand. They are listed in Table I along with other computational parameters.

The translational energy, rotational energy, kinetic energy and gravity potential energy of an ellipsoidal particle are defined as follows:

$$E_{trans} = \frac{1}{2}mv^2 \tag{38}$$

$$E_{rota} = \frac{1}{2}(I_{\bar{x}}\omega_{\bar{x}}^2 + I_{\bar{y}}\omega_{\bar{y}}^2 + I_{\bar{z}}\omega_{\bar{z}}^2) \tag{39}$$

$$E_{kin} = E_{trans} + E_{rota} \tag{40}$$

$$E_{pot} = mg(z - z_{ref}) \tag{41}$$

where $\bar{x}, \bar{y}, \bar{z}$ denote the LCS embedded in the ellipsoidal particle, z denotes the particle centroid height and z_{ref} the reference level. These are calculated as post-processing for each time step to better understand how energy is evolving during the DE simulations. The balance of energy is not solved.

|	
Young's modulus, E (Pa)	2.9×10^{10}
Poisson's ratio, ν	0.25
Specific gravity, G_s	2.65
Interparticle coefficient of friction, μ	0.2-0.7
Interparticle contact damping ratio, ξ	1-5%
Particle radii, m	0.001-0.005
Background damping ratio	0 or DR
Time step, Δt (sec)	5.0×10^{-6}-5.0×10^{-8}

Table I.
Parameters of particles and numerical computation

Notes: Time step covers a large range due to different simulation configurations such as particle size and dropping height

3.1 Centric impact

In this test, an upper particle is allowed to fall freely through gravity and impact centrically upon a lower particle fixed on a table, shown in Figure 5(a). No background damping or interparticle damping is applied so the energy of the system should be conserved. Figure 5(b) illustrates the kinetic energy of the system during the impact, which clearly describes the cyclic process of falling, impacting and rebounding. The vertical line reflects the instant of impact between two particles, whose details are illustrated in Figure 5(c). If the time step Δt is small enough, the line is able to reach the abscissa, capturing the "exact" instant when the top particle's velocity becomes zero. If Δt is larger, conservation of kinetic energy is lost due to inaccuracy of the time integration (assuming it is still small enough to ensure stability of the integration).

Interparticle contact damping influences the energy dissipation substantially. With 5 percent contact damping applied, the system dissipates energy and reaches static
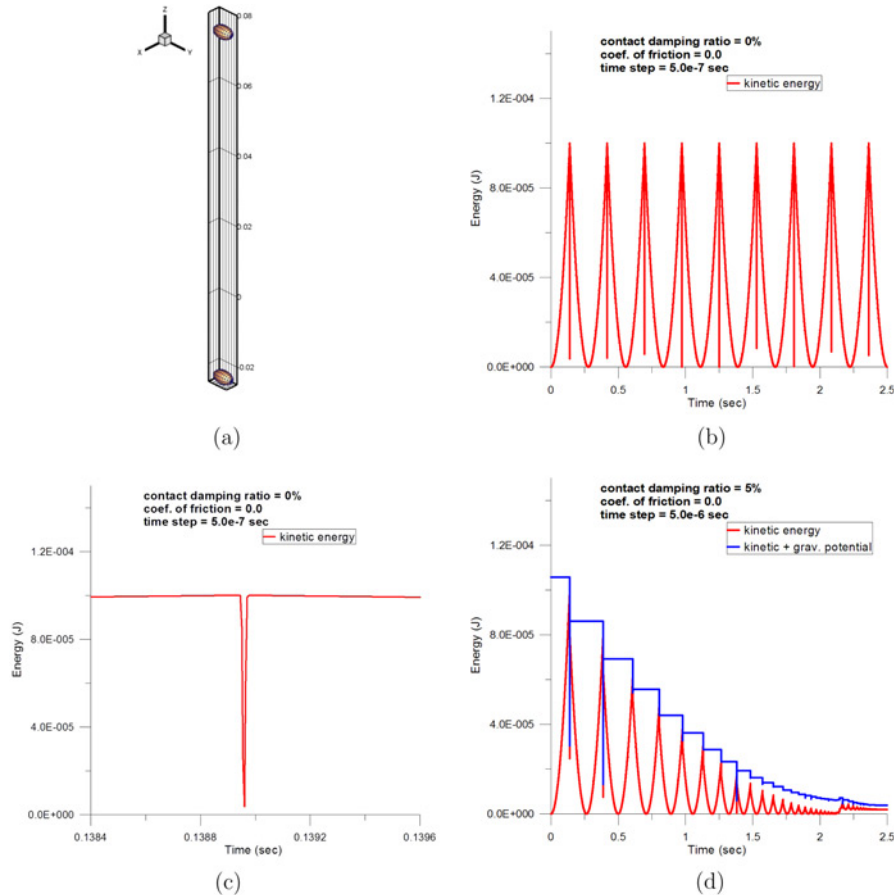
Notes: (a) Initial configuration; (b) kinetic energy; (c) kinetic energy during impact; and (d) energy at 5 percent contact damping

Figure 5.
Two particle centric impact

equilibrium (the top particle stays still on top of the bottom one) quickly in approximately 2 s, shown in Figure 5(d). A small amount of interparticle contact damping (5 percent in the numerical examples) can increase the stable time step for dynamic simulation. For dense, many-particle simulations with significant interparticle sliding, friction will play a dominant role in energy dissipation.
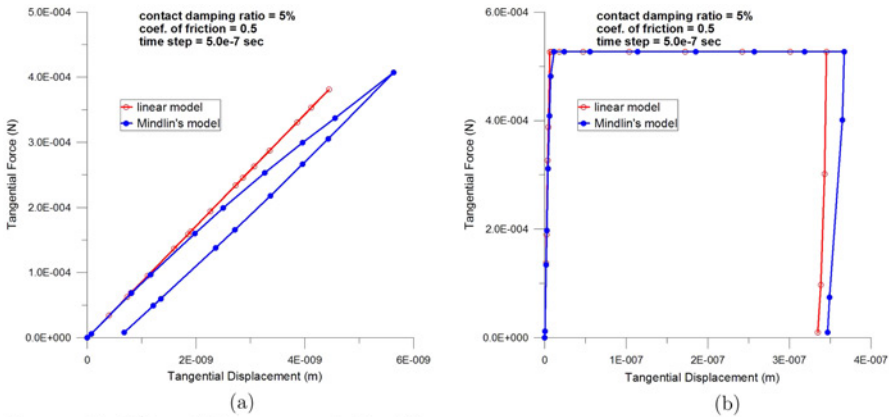
3.2 Tangential behavior at contact
When modeling natural granular materials like sand, friction parameters along with particle shapes (there could be a distribution across a sample) will dictate the mechanical response. Oftentimes, friction accounts for particle surface roughness and some shape angularity that otherwise would be too computationally intensive to resolve spatially for many particle systems (i.e. an ellipsoidal or polyhedral particle shape can only account for so much natural grain angularity). In this test of tangential behavior, a top particle is squeezed upon a bottom one using a constant force N, whereas the bottom one is fixed, disallowing any translational or rotational degree of freedom (DOF), illustrated in Figure 6. A moment is then applied on the top particle, driving it to rotate. The moment is increased and then decreased, allowing the top particle to experience loading and unloading path in the tangential direction. The interparticle coefficient of friction, μ, is assumed to be 0.5.

In Figure 7, the relationship between tangential force and tangential displacement under the constant normal force is illustrated. Figure 7(a) represents the case where the tangential force does not exceed μN and only slip occurs while Figure 7 (b) represents the case where the tangential force exceeds μN and slide occurs.

Linear model and Mindlin model are compared for both adhered/slip and slide situations. On the basis of the assumption that the tangential stiffness of the linear model be evaluated as the no-slip case of Mindlin's equation, the two models only show a minor difference if incremental method is used in calculating the tangential stiffness, because the shear moduli of the two particles are large.
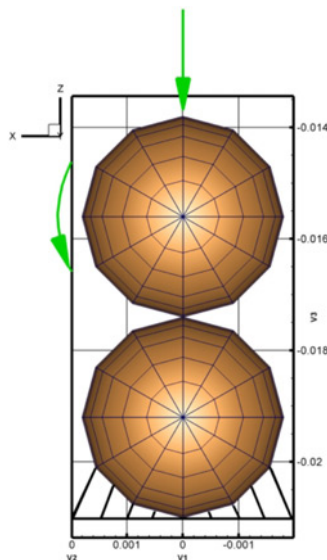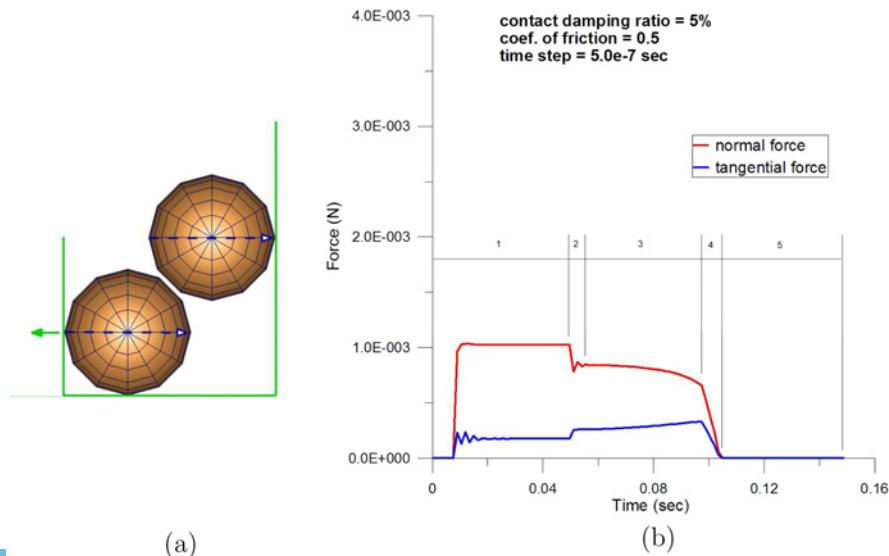

Figure 6.
Particle tangential behavior test configuration

Figure 7.
Tangential force-
displacement relationship
under a constant normal
force using linear and
Mindlin model

Notes: (a) Adhered/slip case and (b) slide

3.3 Rolling and sliding

Rolling and sliding between particles are of great interest in investigating the behavior of frictional granular material. In this test, two particles are placed in equilibrium inside a rigid wall container, illustrated in Figure 8(a). The left wall of the container is removed suddenly and the two particles start to move dynamically.

The simulation indicates that the whole process can be divided into five stages:

(1) two particles reach initial static equilibrium;

(2) the left wall is removed and two particles start to move;

(3) two particles roll upon each other;

(4) two particles slide between each other; and

Notes: (a) Initial configuration and (b) five stages

Figure 8.
Rolling and sliding test

(5) two particles detach, as shown in Figure 8 (b).

The influence of coefficient of friction is tested: if $\mu = 0$, no rotation occurs; if $\mu > 0$, the two particles roll and slide against each other. A larger value of μ results in a larger angle of rotation of the top particle.

3.4 Obliquely oriented ellipsoids in contact
Two obliquely oriented ellipsoids are placed in a rigid wall container to track their motion, contact detectio and energy process. The container size is $10 \times 10 \times 10$ mm. The two particles are $4.0 \times 3.0 \times 1.5$ mm and $4.0 \times 2.0 \times 1.5$ mm in radius, respectively. The interparticle and particle-wall coefficients of friction are assumed to be 0.5 and no background damping is applied. As shown in Figure 9(a), the bigger particle lies on the bottom of the container and the smaller particle drops from a short height to impact the bigger one. Figure 9(b) captures a stage when the two particles are in contact with each other. The two particles translate, roll and slide against each other until both stay at rest finally, i.e. the smaller particle is "locked" between the bigger particle and container walls, shown in Figure 9(c). During this process, the contact
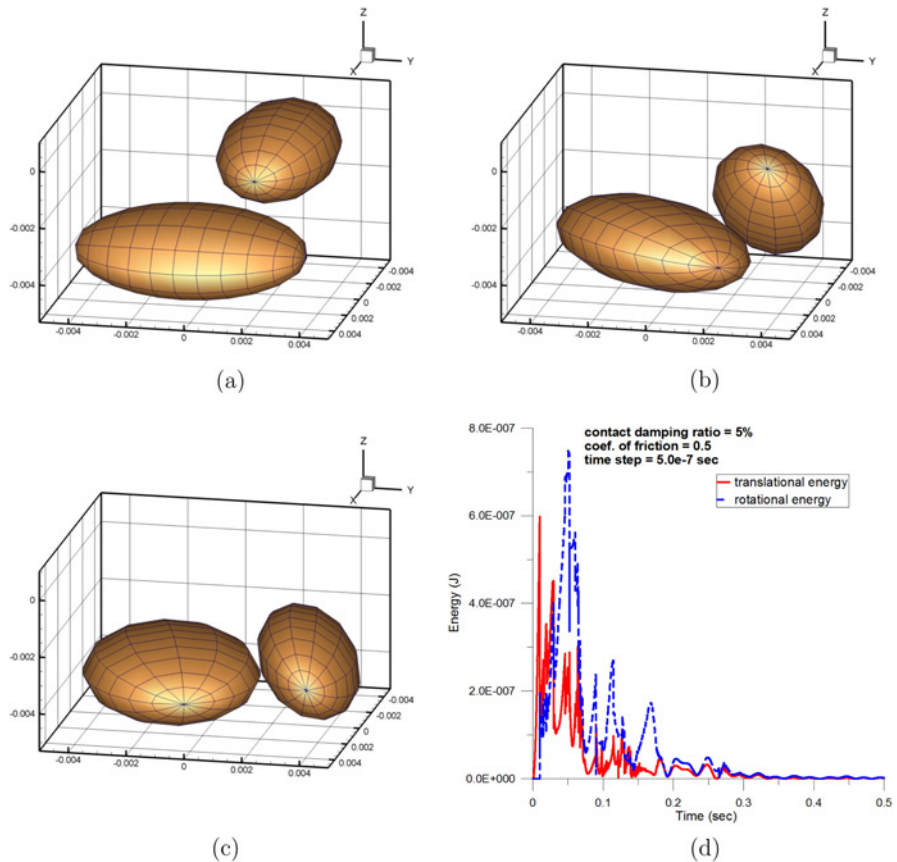
Figure 9.
Two obliquely oriented
ellipsoids in contact

Notes: (a) Initial state; (b) in contact; (c) final state; and (d) energy

points keep changing (the dynamic nature of contact is indicated by the peaks and valleys in energy curves) and ELLIP3D provides a robust algorithm to keep track of them. The energy process of this two-particle system is plotted in Figure 9(d). It can be seen that translational and rotational energy are of the same magnitude in this simulation, and that both normal and tangential interaction between a pair of particles play important roles in dissipating energy.

3.5 Gravitational deposition
As shown in Figure 10(a), a layer of various-sized ellipsoidal particles are released from a certain height into a rigid wall container. The orientations of the particles are randomly generated.

Figure 10(b) illustrates the translational and rotational kinetic energy process during single layer deposition in terms of the following parameters: $\xi = 5$ percent, $\mu = 0.5$, $\Delta t = 5 \times 10^{-7}$ s. It shows that the initial kinetic energy is dominated by translational motion as the particles fall, and then rotation is observed when they contact frictionally at 0.1 s.

Multiple layers of uniform sized ellipsoidal particles are released from a certain height into a rigid flat wall container. The container walls are assumed to have the same friction as between particles. The initial state is shown in Figure 11(a): the orientations of the particles are randomly generated and each particle does not contact any others. The particles begin to deposit through gravitational force with $\xi = 5$ percent and $\mu = 0.5$.

It is worth noting that a significant difference exists between multiple layer deposition and a single layer deposition. These simulations are run without background damping ($\alpha_1 = 0$). In the multiple layer deposition, the particles cannot rebound as freely as those in the single layer deposition in that motion of the lower particles are restrained by the upper particles, i.e. there are many more particle contacts and it tends to result in smaller overlap between particles in an average sense.

(a)   (b)

Notes: (a) Initial configuration and (b) translational and rotational energy
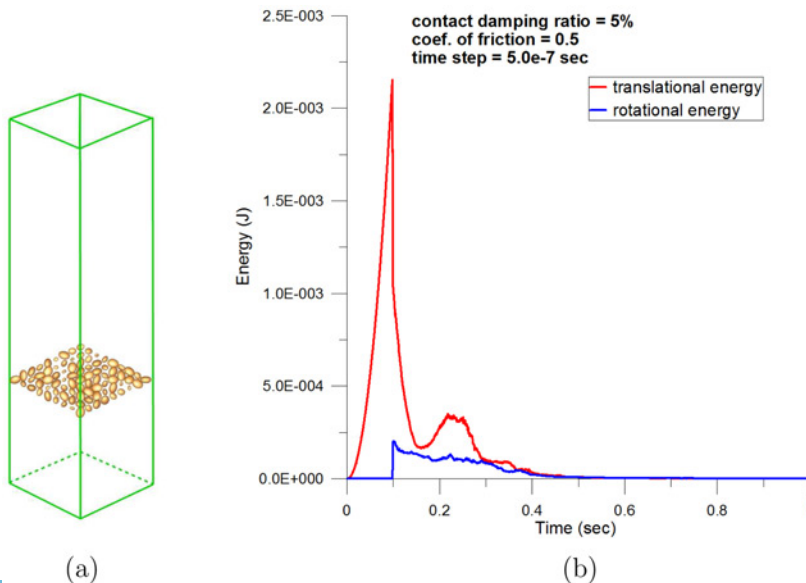
Figure 10.
Single layer dynamic
deposition
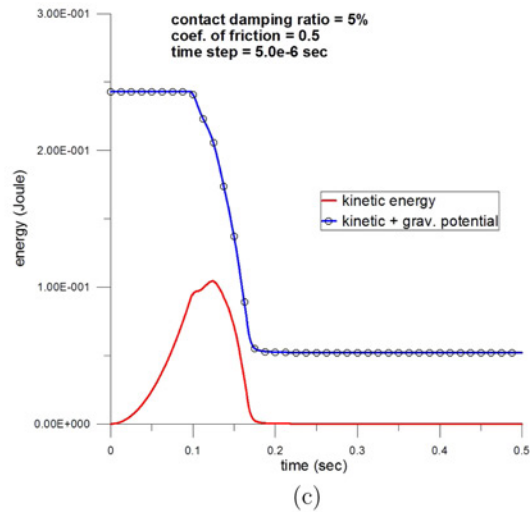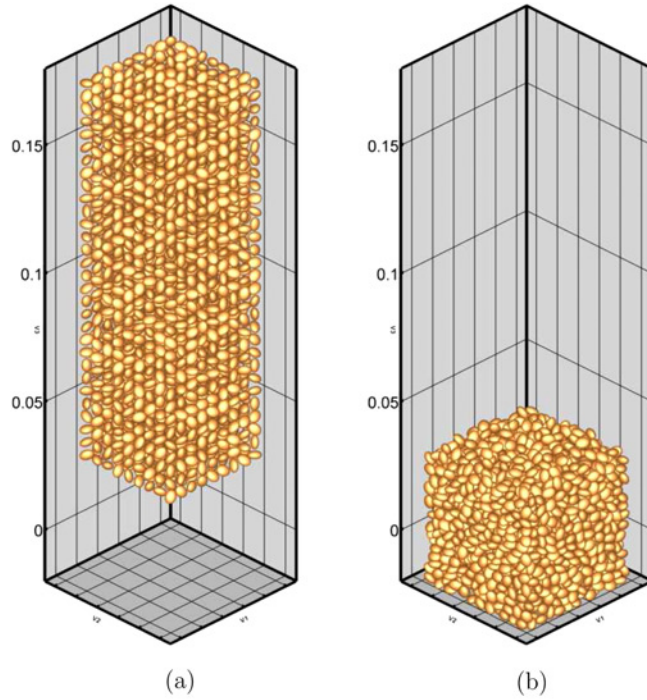
Figure 11.
Multiple layers dynamic
deposition

Notes: (a) Initial state; (b) steady state; and (c) energy process

From Equations (29) and (9), it can be seen that a smaller penetration between particles results in a smaller normal stiffiness, which in turn leads to a larger allowable time step. Based on this phenomenon, a larger time step can be employed in the computation, which is valuable for simulations with a large amount of particles.

Energy curves of multiple layer deposition are illustrated in Figure 11(c). Compared to Figure 10(b), it can be observed that the particles move much less intensively in multiple layer deposition. Only the top layer of particles are able to rebound freely, and it takes additional time for those particles to come to rest. The deposited final steady state configuration shown in Figure 11 (b) is used for the following quasi-static simulations.
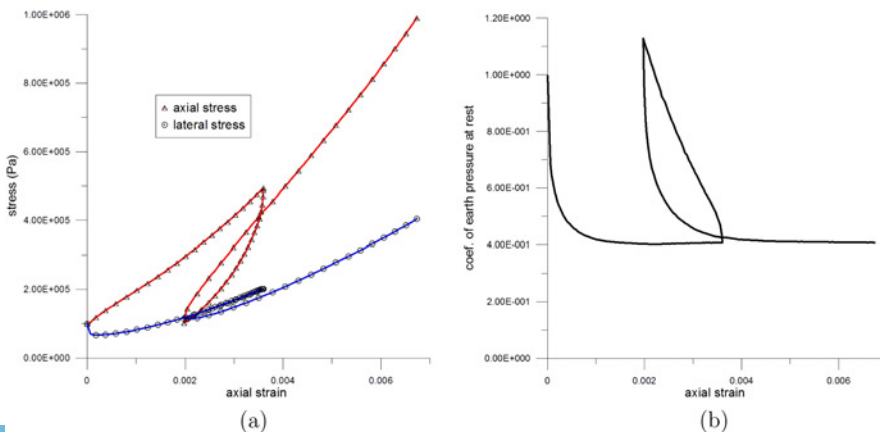
3.6 Oedometer compression
It should be pointed out that:

(1) All the oedometer compression, triaxial compression and pile penetration are quasi-static simulations using DR method, and the pile penetration uses particle mass scaling and gravity scaling.

(2) The stress on each wall of the container is calculated by averaging particle-wall contact forces over the wall area, which allows a precise equlibrium control during the simulation.

An oedometer compression (uniaxial strain) is simulated on the sample deposited by gravity in Figure 11(b) with loading-unloading-reloading path. Figure 12(a) illustrates the relationship between axial stress/lateral stress and volumetric strain during the test. The coefficient of lateral earth pressure, $K_0 = \sigma_{\text{lateral}}/\sigma_{\text{axial}}$, is plotted in Figure 12(b). It is observed that K_0 drops from the initial value 1.0 and stays stable at around 0.45 in the test, which is a typical average value for normally consolidated sands. During the path of unloading-reloading, it increases and decreases correspondingly and then goes back to 0.45. It is interesting that K_0 goes up to 1.13 in the unloading process, which means axial stress is lower than the lateral stress at that instant. The particles may be laterally "locked" by the container when the axial stress is released. A significantly lower K_0 during reloading than during unloading has been found in laboratory tests on a uniform medium sand (Al-Hussaini and Townsend, 1975), which is replicated qualitatively in this numerical test.

3.7 Triaxial compression
Triaxial compression tests are conducted with various confining pressures, which covers a wide range from 100 to 3,500 kPa. The confining pressure is applied on the six

Notes: (a) Stress vs axial strain and (b) coefficient of earth pressure at rest vs axial strain

Figure 12.
Oedometer compression
with load-unload-
reload path

www.mana

boundaries of the specimen and then displacement-controlled BCs are applied at the top and bottom platens. Figure 13 illustrates cross-sectional view of the specimen, where the deformation is demonstrated clearly as well as the particle contact state.

Figure 14(a) and (b) illustrate the stress-strain relationship and volumetric behavior in the triaxial compression simulation with various confining pressures, respectively. It displays a trend of dilatancy for an initially dense sample: the volume of the specimen contracts first and then expands as axial strain increases. Qualitatively, it agrees with the triaxial test results (Jernigan, 1998) where 4-8 mm Sweden Ballast was used as oversized granular soils.

Figure 14(c) displays the curves of average coordination number along with the axial strain change. They look like typical stress-strain curves of dense sand in triaxial test. Coordination number increases during compaction and decreases during dilation. Compared with Figure 14(a), the coordination number varies in advance of the deviator stress.

The relationship between void ratio and deviator stress is illustrated in Figure 14(d), which demonstrates dilatancy. The lower confining pressure specimens dilate more than the higher confining pressure ones. Qualitatively it agrees well with laboratory curves (Hirschfeld and Poulos, 1963).

### 3.8 Pile penetration with fixed boundary

A simplistic pile penetration test is simulated quasi-statically to demonstrate boundary effects. The pile is modeled using a relatively large ellipsoidal particle, and the boundaries are composed of spatially fixed spherical particles, illustrated in Figure 15(a) and (b). As shown in Figure 15(c), three different-sized containers are used, number of particles being 2,760, 4,260 and 6,088, respectively. The dimension of free particle deposited in the container is $2.5 \times 2.0 \times 1.5$ mm in radius and the three container horizontal dimensions are 39.6×39.6 mm, 49.5×49.5 mm and 59.4×59.4 mm, respectively. The height of deposited particle assembly inside the container is 83 mm.

The vertical force-displacement curves are plotted in Figure 16 for the pile particle. It can be found that the pile force increases as penetration increases. For a smaller container, the force has a larger value because of the boundary effect, as expected.
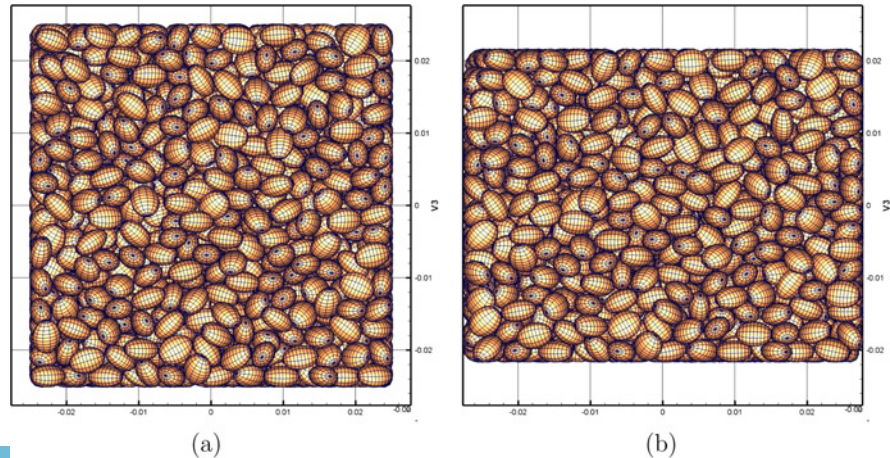
Figure 13.
Cross-sectional view of triaxial compression

(a)   (b)

Notes: (a) Initial state and (b) final state
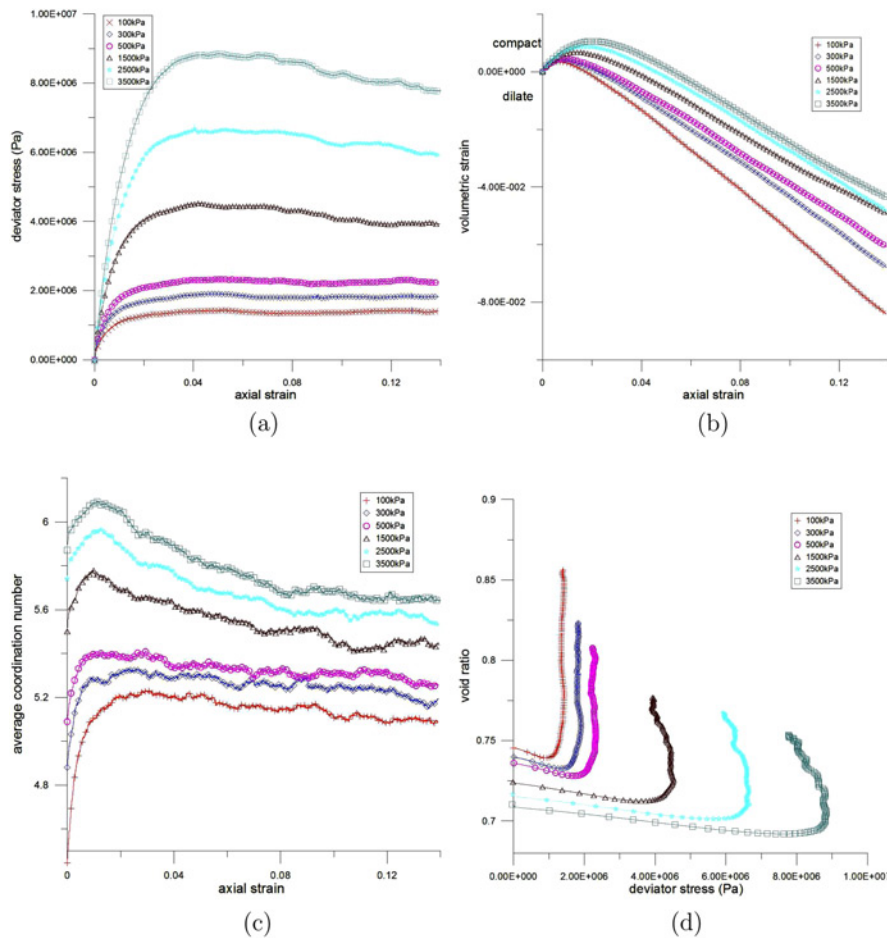
Notes: (a) Deviator stress vs axial strain; (b) volumetric strain vs axial strain; (c) coordination
number vs axial strain; and (d) void ratio vs deviator stress

4. Discretre element/finite element facet coupling

To solve fracture or penetration mechanics problems computationally efficiently with
higher-fidelity materials models, various multiscale approaches have been developed.
These multiscale methods couple particle methods to continuum methods via an
overlapping, or "hand-shaking", region. Examples of such approaches have been
demonstrated for coupled atomistic-continuum regions (Wagner and Liu, 2003; Xiao
and Belytschko, 2004; Klein and Zimmerman, 2006), to name a few.

The differences between atomistic-continuum coupling and granular-continuum
coupling should be noted:

- MD simulations are widely used because of the availability of accurate
  interatomic potentials for lattice-structured materials. Granular particles interact
  with each other through contact and friction, making such potentials not
  applicable to granular materials.

(a)

(b)

(c)
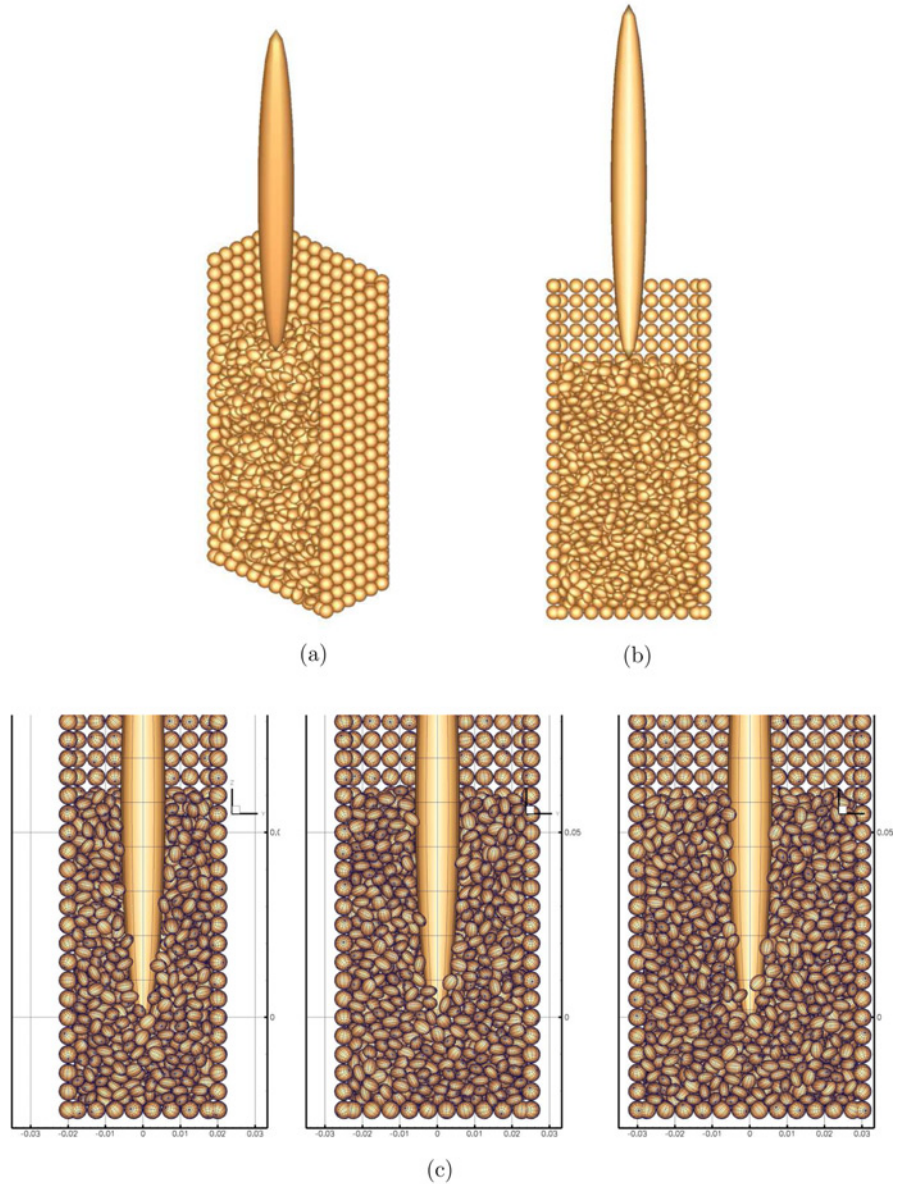
Figure 15.
Cross-sectional view of
pile penetration

Notes: (a) 3D view; (b) 2D view; and (c) different sized containers

- Granular materials are generally "frictional" materials (assumed cohesionless).
  The assemblies of granular materials deform with the change of BCs. If no BC is
  applied (i.e. unconfined), the assemblies could become individual particles
  without any contact interaction (i.e. falling or floating in space) or obtain an
  angle of repose under gravity loading. Due to their "frictional" nature, particle
  shape and grain size distribution influence the mechanical behavior
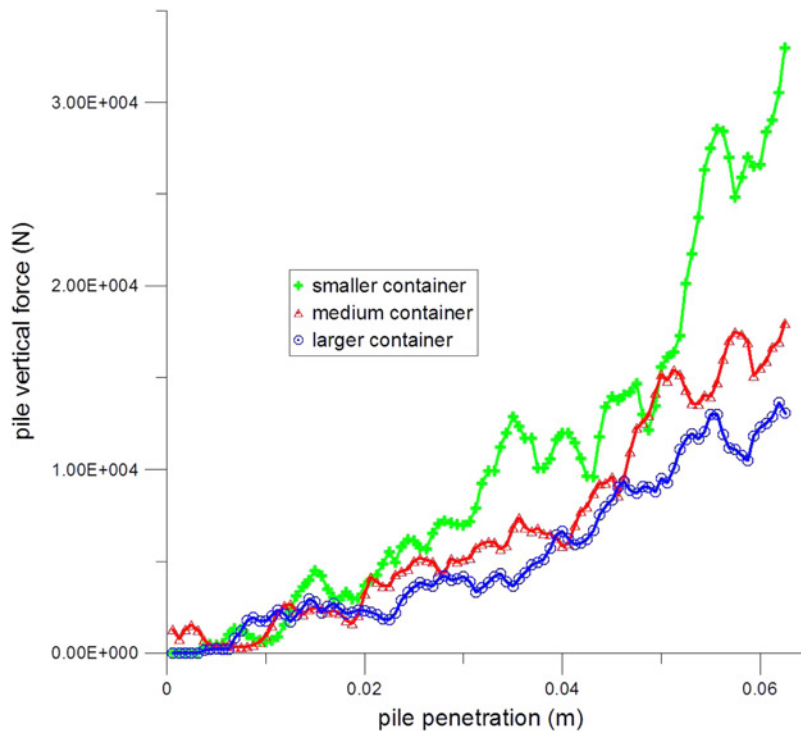
Figure 16.
Pile force-displacement
curves with different
sized containers

dramatically. For lattice-structured materials, they have regular atomic structure
and can retain their shape without confinement.

- Rotation and shape of granular particles play an important role in determining
  the deformation and strength of assemblies. This is not the case with atoms in
  MD (although structure of a molecule will be important in MD).

- The reduction of MD DOF in atomistic-continuum coupling is made possible as a
  result of the periodic nature of crystal lattices. Collections of atoms called the unit
  cell is repeated in exactly the same arrangement over and over throughout the
  entire material; this is not true with granular materials, which are generally
  highly heterogeneous at their particle-scale.

- Granular materials may undergo large shear deformation and/or particle flow
  which prevents a FE mesh from covering the entire domain in a simulation (large
  distortion of FE mesh requires adaptive re-meshing). For example, when a
  square pre-stressed concrete pile is driven 5 m vertically into a sand foundation,
  the pile displaces the sand media with its body occupying physical space, which
  would cause a FE mesh covering the penetration region to be re-meshed many
  times (something to be avoided for computational efficiency). Within that
  domain, pure DE simulation could be used to resolve properly the underlying
  physics, while outside that domain FE simulation can be adopted for proper BCs
  on the DE domain, and computational efficiency.

On the basis of above comparison and analysis, a simple granular-continuum coupling scheme is proposed initially, illustrated in Figure 17. The FE mesh does not cover the entire domain. Instead, the FE region and DE region only overlap through a single layer of particles. This layer of particles is embedded on the surface of the FE domain with centroids constrained to FE facets and deform with FE mesh. We call these particles "ghost" particles, as done in atomistic-continuum coupling methods. The hand-shaking area is downgraded to a layer of ghost particles, and there is no overlap, thus providing only a preliminary code communication between ELLIP3D and TAHOE. Theoretically, the ghost particles can comprise multiple layers and extrude into/overlap with the FE mesh, but this is left for future work (Regueiro, 2007; Regueiro and Yan, 2009). No energy partitioning is currently considered. Only force and kinematics are communicated between the FE and DE regions through the single layer of ghost particles constrained to follow the motion of the FE facets to which they are tied.

Depending on the FE type, the ghost particles may or may not maintain rotational DOF. Ideally, when a micropolar or micromorphic continuum model (Regueiro, 2009) is used within the FE region, the ghost particles will have rotational DOF. If conventional FEM is adopted (like in this paper), the ghost particles have constrained rotational DOF. Free particles in the DE domain carry both translational and rotational DOF.

The computational framework involves a two-way exchange of information: free particles in the DE simulation contribute to the boundary force in the FE domain through ghost particles, the FE domain provides information needed to compute the BC on the free particles through ghost particles as well. The granular and continuum scales run simultaneously and exchange relevant information dynamically.
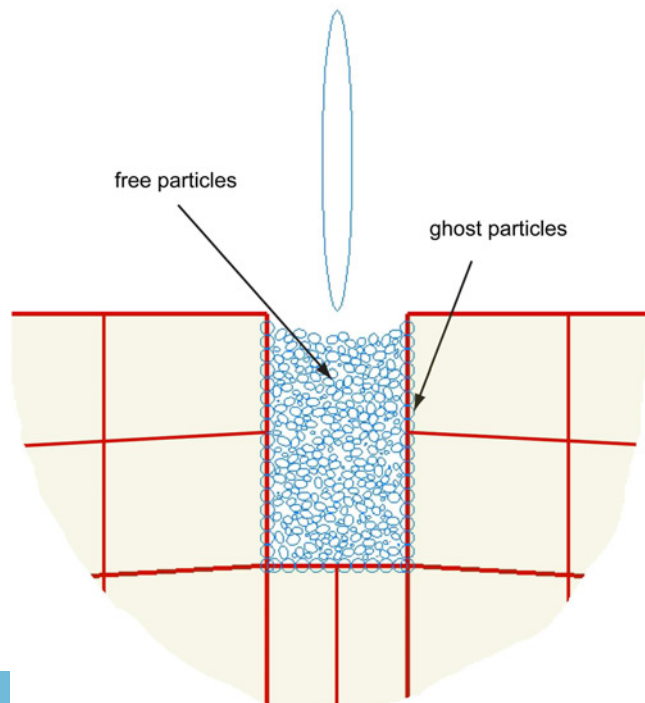
Figure 17.
Schematic illustration of simple granular-continuum coupling

The ghost particles are embedded on the surfaces of the FE domain and transfer forces from DE domain to FE domain through the coupled FE facets. The ghost particles can be placed in such a manner that their centroids are exactly located on the surface FE facets. As ghost particles are discrete in space, the forces are discrete in space as well. Each force acts like a point load on the FE mesh, not necessarily acting at a FE node. When a point force P acts in the interior (including boundary) of the element domain, the relation between the distributed force $b(x)$ at point x and the point force can be denoted mathematically as:

$$b(x) = P\delta(x - a) \tag{42}$$

where $\delta(x - a)$ is the Dirac delta function and $x = a$ the location of force action P. The Dirac delta function has the property that for any vector function $g(x)$:

$$\int_\Omega g(x)\delta(x - a)dx = \begin{cases} g(a), & a \in \Omega \\ 0, & \text{otherwise} \end{cases} \tag{43}$$

Thus, the external nodal forces on an element e arising from a point force P at a can be obtained by:

$$\begin{aligned} f^e &= \int_\Omega N^{eT}(x)b(x)dv \\ &= \int_\Omega N^{eT}(x)P\delta(x - a)dv \\ &= \begin{cases} N^{eT}(a)P, & a \in \Omega \\ 0, & \text{otherwise} \end{cases} \end{aligned} \tag{44}$$

where N^e is the matrix of FE shape functions for element e. Extending it to all FE over the entire domain we have:

$$f = N^T P \tag{45}$$

When the FE mesh deforms, the ghost particles move as well, maintaining their centroids on the surface of the FE mesh. Usually, the ghost particles are initially setup such that their centroids coincide with FE mesh surface. Their centroid locations need to be mapped from global coordinates to local element natural coordinates using a Newton-Raphson iterative method. Once the natural coordinates are determined, the locations of ghost particles can be evaluated using the following relationship through shape functions $N_{\widehat{Q}D}$ during the subsequent simulation:

$$\widehat{Q} = N_{\widehat{Q}D} D \tag{46}$$

where $\widehat{(\bullet)}$ denotes prescribed particle DOFs.

The following list summarizes the algorithm to implement the granular-continuum coupling scheme:

- Initialize DE and FE domain.
- If simulation steps are reached, stop; otherwise continue.

- Run DE simulation with ghost particles at boundary and calculate forces that each ghost particle is subjected to.
- Apply ghost particle forces to FE using $\boldsymbol{f} = \boldsymbol{N}^T \boldsymbol{P}$.
- Run FE simulation.
- Update ghost particle motion using $\widehat{\boldsymbol{Q}} = \boldsymbol{N}_{\widehat{QD}} \boldsymbol{D}$.
- Return to Step 2.

In practice, DE code ELLIP3D is wrapped and integrated into FE code TAHOE (tahoe.ca.sandia.gov) using object-oriented programming methodology for the algorithm implementation.

5. Discrete element/finite element coupling simulation examples

5.1 Benchmark test

As a benchmark, an elastic cube ($E = 5.0 \times 10^7 \, \text{N/m}^2$, $\nu = 0.2$) modeled with eight trilinear hexahedral elements is studied with two cases: the first is to apply a vertical point force directly at the center of its top surface; the second is to place four ghost particles around its top central node and use a free particle to apply force to the four ghost particles. The dimension of the cube is 0.2 m. The radii of the spherical ghost particles and the free particle are 1.5 and 3.0 mm, respectively, see Figure 18. The

(a)

(b)

(c)
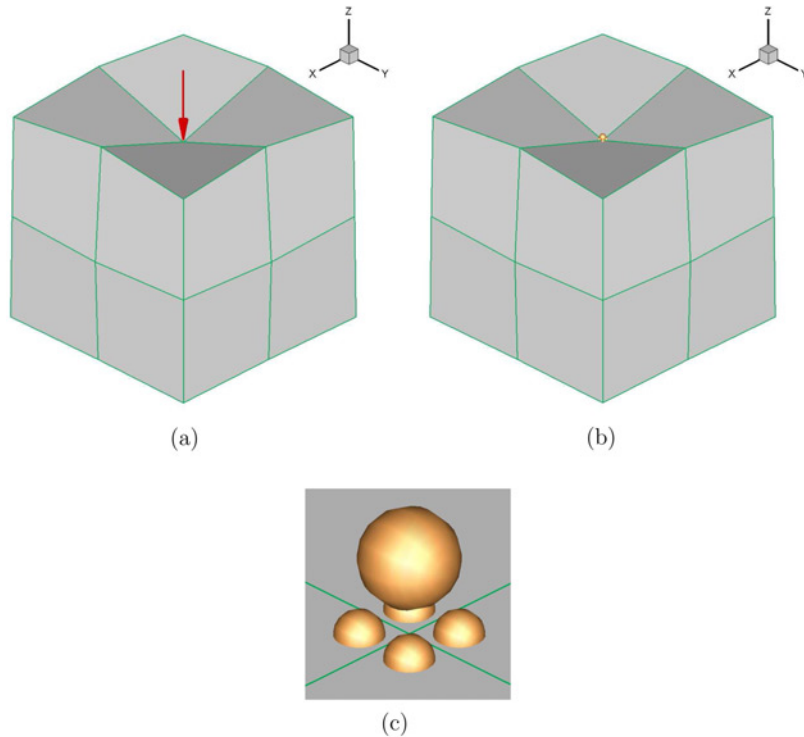
Figure 18.
A benchmark test on cube deformation

Notes: (a) Pure FEM test; (b) DE-FE coupling test; and (c) particles configuration

magnitudes of the vertical point force and the free particle gravity are assumed to be the same, 1.0×10^5 N.

The two cases give close results as shown in Figure 18(a) and (b). The difference can be explained: in the first case, the point force is undertaken by the top central node, while in the second case the gravity of the free particle is undertaken by the top central node and its surrounding nodes on the top four elements through the concentrated FE facet particle force distribution in Equation (44).

When the four ghost particles move closer to the top central node, the result gets closer to that of the single point load. As the four ghost particles are all placed exactly at the top center (and thus they are completely overlapped), the deformation of the cube converges to the same result as that resulting from a single point force.

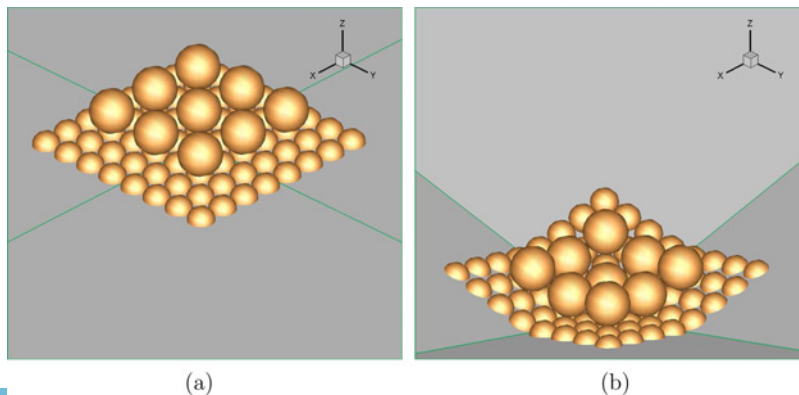### 5.2 Ghost particles motion
It is important to guarantee that ghost particles move with the deformation of an FE mesh. A test with 64 ghost particles and 9 free particles is carried out to examine ghost particle movement. As the cube deforms, it is observed that ghost particles move with the FE facets, captured in Figure 19.

5.3 Pile penetration with coupled FE facets
The particles from the pile penetration example with smaller "container" are combined with a FE domain, shown in Figure 20.

As the pile is driven into the free particles, the ghost particles are squeezed outwards towards the FE domain. Figure 21 depicts the pile-induced displacement field of all ghost particles (rotations fixed because FE continuum is non-polar). It is noteworthy that the "container" formed by ghost particles swells at lower part, similar to the influence region for pile excitation problems (Ashlock, 2006).

To examine the effect of DE-FE coupling on force-displacement curves of pile penetration, the small container curve and large container curve in Figure 16 are plotted again, together with the curve obtained from small container with DE-FE coupling, shown in Figure 22. It is observed that the pile force of the small container with DE-FE coupling can be tuned to match the larger container with no coupling, by
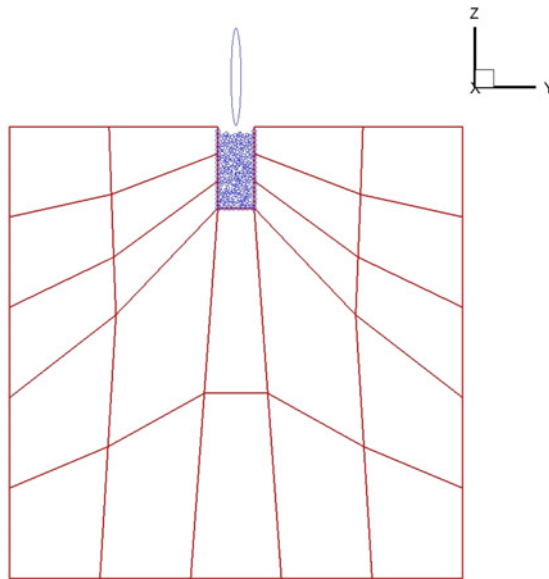

(a)   (b)

Notes: (a) Initial state; (b) final state; 64 ghost particles and nine free particles

Figure 19.
Details of ghost particles
moving with FE
deformation

Figure 20.
3D view of the DE and
FE domain
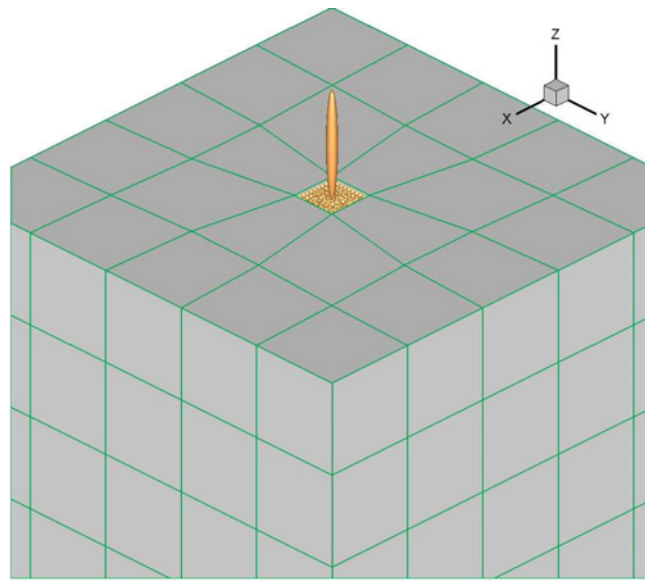
Notes: (a) Opaque view and (b) cross-sectional view

adjusting the elastic compliance of the FE continuum surrounding the container. The boundary effect difference is shown in Figure 16 can be partially or completely eliminated by applying a more robust DE-FE coupling technique in future work, similar to the atomistic-continuum coupling methods, but accounting for differences
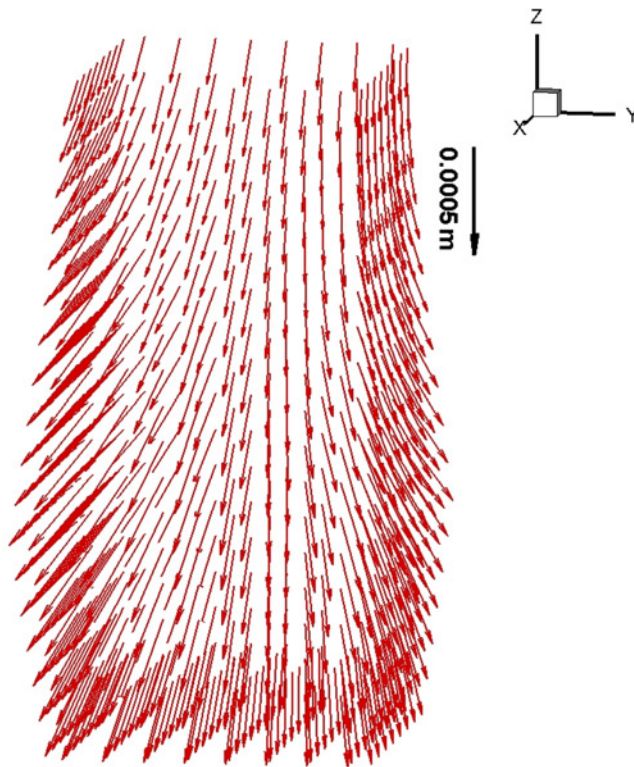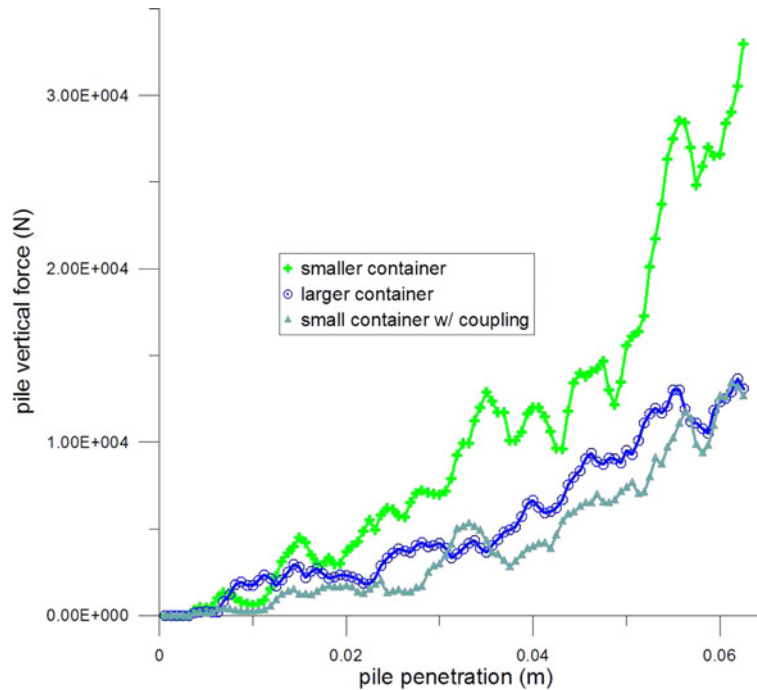
Figure 21.
Pile-induced displacement
field of ghost particles

with granular materials (see discussion at beginning of section 4). Such work is ongoing.

6. Conclusions
The development of a 3D ellipsoidal DE code ELLIP3D enables us to study the fundamental mechanical behavior at particle contact as well as simulate granular particle assembly response under various conditions. It is found that a linear model and Mindlin's model only show a minor difference under the small contact deformation assumption for stiff particles. Results from oedometer and triaxial compression agree qualitatively with laboratory data.

Coupling DE to FE domains to reduce computational cost is realized through a layer of "ghost" particles embedded on surface FE facets. Pile penetration simulations show that the artifical boundary effect can be alleviated by using the coupled FE facets with tuned FE continuum elastic compliance. The granular-continuum coupling technique and its extension to more robust overlapping bridging scale methods in future work can be expected to be an effective method in providing a nearly seamless DE-FE transition and lowering computational cost associated with granular material/ deformable solid body interfaces, such as encountered, for example, for granular soil-tool, tire, penetrometer, pile interfaces.

Figure 22.
Comparison of pile force-displacement curves

References

Al-Hussaini, M. and Townsend, F. (1975), *Investigation of k_O Testing in Cohesionless Soils*, final report, Army Engineer Waterways Experiment Station, Vicksburg, MS.

Ashlock, J. (2006), "Computational and experimental modeling of dynamic foundation interactions with sand", technical report, PhD thesis, University of Colorado, Boulder, CO.

Cheng, H.-X., Gong, X., Guo, X.-L., Dai, Z.-H., Chen, F. and Xiong, L. (2005), "Mathematic model analysis of powder flow in hopper", *Huaxue Gongcheng*, Vol. 33 No. 3, pp. 33-5.

Cook, B. and Jensen, R. (2002), *DEM: Numerical Modeling of Discontinua*, ASCE Geotechnical Special Publication No. 117, Reston, VA.

Cundall, P. and Strack, O. (1979), "A discrete numerical model for granular assemblies", *Geotechnique*, Vol. 29, pp. 47-65.

Gong, L. (2001), "Discrete element modeling of three-dimensional assemblies of ellipsoidal particles", technical report, PhD Thesis, University of Colorado, Boulder, CO.

Han, K., Peric, D., Crook, A. and Owen, D. (2000), "A combined finite/discrete element simulation of shot peening processes. Part I: studies on 2D interaction laws", *Engineering Computation*, Vol. 17 No. 2, pp. 593-619.

Hertz, H. (1882), "Ueber die Berührung fester elastischer Körper" ("On the fixed elastic body contact"), *Journal für die reine und angewandte Mathematik (Crelle)*, Vol. 92, pp. 156-71.

Hirschfeld, R. and Poulos, S. (1963), "High-pressure triaxial tests on a compacted sand and an undisturbed silt", *Laboratory Shear Testing of Soils*, pp. 329-41, ASTM, Philadelphia, PA.

Hopkins, M. (2002), "Discrete element modeling based on mathematical morphology", in *Discrete Element Methods: Numerical Modeling of Discontinua*, Sante, Fe, NM, No. 117, pp. 38-41.

Hopkins, M. (2004), "Discrete element modeling with dilated particles", *Engineering Computations*, Vol. 21 Nos 2-4, pp. 422-30.

Jernigan, R. (1998), "The physical modeling of soils containing oversized particles", technical report, PhD thesis, University of Colorado, Boulder, CO.

Johnson, S., Williams, J.R. and Cook, B. (2004), "Contact resolution algorithm for an ellipsoid approximation for discrete element modeling", *Engineering Computations*, Vol. 21 Nos 2-4, pp. 215-34.

Key, S.W., Stone, C.M. and Krieg, R.D. (1980), "Dynamic relaxation applied to the quasi-static, large deformation, inelastic response of axisymmetric solids", ERDA/420200, SAND801605C, Sandia National Laboratories Report, CONF-800781-1, Albuquerque, NM.

Klein, P. and Zimmerman, J. (2006), "Coupled atomistic-continuum simulations using arbitrary overlapping domains", *Journal of Computational Physics*, Vol. 213 No. 1, pp. 86-116.

Komodromos, P. and Williams, J. (2002), "On the simulation of deformable bodies using combined discrete and finite element methods", *Geotechnical Special Publication*, Vol. 1 No. 117, pp. 138-44.

Komodromos, P. and Williams, J. (2004), "Dynamic simulation of multiple deformable bodies using combined discrete and finite element methods", *Engineering Computations*, Vol. 21 Nos 2-4, pp. 431-48.

Kremmer, M. and Favier, J. (2001), "A method for representing boundaries in discrete element modeling – Part I: geometry and contact detection", *International Journal for Numerical Methods in Engineering*, Vol. 51 No. 12, pp. 1407-21.

Kuhn, M. (2003), "Smooth convex three-dimensional particle for the discrete-element method", *Journal of Engineering Mechanics*, Vol. 129 No. 5, pp. 539-47, available at: http://dx.doi.org/10.1061/(ASCE)0733-9399(2003)129:5(539)

Lin, X. and Ng, T.-T. (1995), "Contact detection algorithms for three dimensional ellipsoids in discrete element modeling", *International Journal for Numerical and Analytical Methods in Geomechanics*, Vol. 19 No. 9, p. 653.

Lipschutz, M. (1969), *Schaum's Outline of Differential Geometry*, 1st ed., McGraw-Hill, New York, NY.

Liu, W.K., Karpov, E.G. and Park, H.S. (2006), *Nano Mechanics and Materials: Theory, Multiscale Methods, and Applications*, 1st ed., John Wiley & Sons, Chichester.

Mindlin, R. (1949), "Compliance of elastic bodies in contact", *Transactions of the ASME, Journal of Applied Mechanics*, Vol. 16 No. 3, pp. 259-68.

Mindlin, R. and Deresiewicz, H. (1953), "Elastic spheres in contact under varying oblique forces", *Transactions of the ASME, Journal of Applied Mechanics*, Vol. 20 No. 3, pp. 327-44.

Mindlin, R., Mason, W., Osmer, T. and Deresiewicz, H. (1952), "Effects of an oscillating tangential force on the contact surfaces of elastic spheres", *Proceedings of the 1st US National Congress of Applied Mechanics*, Chicago, IL, pp. 203-8.

Nakashima, H. and Oida, A. (2004), "Algorithm and implementation of soil-tire contact analysis code based on dynamic FE-DE method", *Journal of Terramechanics*, Vol. 41 Nos 2/3, pp. 127-37.

Negi, S., Jofriet, J. and Lu, Z. (1999), "Coupled discrete element-finite element model for simulation of bulk solids flow in bins", *Powder Handling Process*, Vol. 11 No. 4, pp. 413-20.

Ng, T.-T. (1993), "Numerical simulations for penetration process of concrete target using the discrete element method", *American Society of Mechanical Engineers, Applied Mechanics Division (AMD)*, Vol. 171, pp. 17-24.

Ng, T.-T. (1994), "Numerical simulations of granular soil using elliptical particles", *Computers and Geotechinics*, Vol. 16 No. 2, pp. 153-69, available at: http://dx.doi.org/10.1016/0266-352X(94)90019-1

Ng, T.-T. (1999), "Fabric study of granular materials after compaction", *Journal of Engineering Mechanics, ASCE*, Vol. 125 No. 12, pp. 1390-94, available at: http://dx.doi.org/10.1061/(ASCE)0733-9399(1999)125:12(1390)

Ng, T.-T. (2004), "Triaxial test simulations with discrete element method and hydrostatic boundaries", *Journal of Engineering Mechanics*, Vol. 130 No. 10, pp. 1188-94, available at: http://dx.doi.org/10.1061/(ASCE)0733-9399(2004)

Ng, T.-T. and Fang, H. (1995), "Cyclic behavior of arrays of ellipsoids with different particle shapes", *American Society of Mechanical Engineers, Applied Mechanics Division (AMD)*, Vol. 201, pp. 59-70.

Onate, E. and Rojek, J. (2004), "Combination of discrete element and finite element methods for dynamic analysis of geomechanics problems", *Computer Method in Applied Mechanics and Engineering*, Vol. 193 Nos 27-29, pp. 3087-128.

Press, W. (2007), *Numerical Recipes, 3rd Edition: The Art of Scientific Computing*, 3rd ed., Cambridge University Press, New York, NY.

Regueiro, R. (2007), "Coupling particle to continuum regions of particulate materials", *Proceedings of the IMECE2007, No. 42717, Seattle, WA*, pp. 1-6.

Regueiro, R. (2009), "Finite strain micromorphic pressure-sensitive plasticity", *Journal of Engineering Mechanics, ASCE*, Vol. 135, pp. 178-91.

Regueiro, R. and Yan, B. (2009), "Concurrent multiscale computational modeling for dense dry granular materials interfacing deformable solid bodies", *Springer Series in Geomechanics and Geoengineering*, Springer-Verlag, New York, NY.

Rothenburg, L. and Bathurst, R. (1992), "Micromechanical features of granular assemblies with planar elliptical particles", *Geotechnique*, Vol. 42 No. 1, pp. 79-95.

Sokolnikoff, I. (1939), *Advanced Calculus*, 1st ed., McGraw-Hill Book Company, New York, NY and London.

Somasundaram, D. (2004), *Differential Geometry: A First Course*, 1st ed., Alpha Science International, Harrow.

Taylor, L.M. and Preece, D.S. (1992) "Simulation of blasting induced rock motion using spherical element models", *Engineering Computations*, Vol. 9 No. 2, pp. 243-52.

Underwood, P. (1983), "Dynamic relaxation", in Belytschko, T. and Hughes, T. (Eds), *Computational Methods for Transient Analysis*, Amsterdam, pp. 245-65.

Vu-Quoc, L., Lesburg, L. and Zhang, X. (2004), "An accurate tangential force-displacement model for granular-flow simulations: contacting spheres with plastic deformation, force-driven formulation", *Journal of Computational Physics*, Vol. 196 No. 1, pp. 298-26, available at: http://dx.doi.org/10.1016/j.jcp.2003.10.025

Wagner, G. and Liu, W. (2003), "Coupling of atomistic and continuum simulations using a bridging scale decomposition", *Journal of Computational Physics*, Vol. 190 No. 1, pp. 249-74.

Wang, C.-Y., Wang, C.-F. and Sheng, J. (1999), "Packing generation scheme for the granular assemblies with 3D ellipsoidal particles", *International Journal for Numerical and Analytical Methods in Geomechanics*, Vol. 23 No. 8, pp. 815-28.

Xiao, S. and Belytschko, T. (2004), "A bridging domain method for coupling continua with molecular dynamics", *Computer Method in Applied Mechanics and Engineering*, Vol. 193 Nos 17-20, pp. 1645-69.

Zhang, R. (1996), "Discrete element modeling of granular materials under biaxial conditions", technical report, PhD thesis, University of Colorado, Boulder, CO.

Corresponding author
Richard A. Regueiro can be contacted at: regueiro@colorado.edu